Check for updates

Effects of the recognition sites of MOFs on turn-off fluorescence detection of Fe³⁺†

Senlin Li,[a] Yanan Gu,[a] Bo Zhao,[a] Haocheng Cai,[a] Zhuo Zhao,[a] Qiaozhen Sun 🔟 *[a] and Bingguang Zhang*[b]

In this work, two fluorescent Cd(II)-based metal–organic frameworks (MOFs), named [CdL(dpa)]·2.5H$_2$O (**1**) and Cd$_2$L$_2$(2,2'-bpy)$_2$ (**2**) (H$_2$L = 5-[(dimethylamino)thioxomethoxy]-1,3-benzenedicarboxylic acid, dpa = 4,4'-dipyridylamine and 2,2'-bpy = 2,2'-bipyridine), were successfully exploited as fluorescent sensors for the detection of Fe³⁺ in an aqueous medium. Compound **1** was assembled with Cd²⁺, L²⁻ and dpa to construct a porous two-dimensional layer. The (dimethylamino)thioxomethoxy groups in the layer protrude into the adjacent layers to form an interdigitated motif. Compound **2** exhibited an infinite ladder-like chain with the (dimethylamino)thioxomethoxy groups hanging on the two sides of the chain. Fluorescence studies revealed that both **1** and **2** can effectively detect Fe³⁺ in H$_2$O through luminescence quenching (K_{sv} = 2.96 × 10⁴ M⁻¹ and LOD = 6.40 × 10⁻⁵ mM for **1**; K_{sv} = 3.31 × 10⁴ M⁻¹ and LOD = 7.65 × 10⁻⁵ mM for **2**). The synergistic competitive absorption and coordination interaction mechanism could explain the detection of Fe³⁺. Furthermore, the enlarged steric hindrance in compound **1** resulted in lower values of K_{sv} and LOD than those of compound **2**, which impeded the coordination of Fe³⁺ with its N, O and S recognition sites.

Introduction

The quality of water is a basic prerequisite for the survival of human beings. Pollutants such as heavy metal ions, pesticides and toxic nitroaromatic compounds present in the water system pose serious threats to human health.[1–3] Therefore, the efficient monitoring of harmful or toxic substances in water resources is requisite and imperative.[4,5]

Metal–organic frameworks (MOFs), comprising organic linkers and inorganic metal nodes (or clusters), find applications in many fields owing to their facile tuned structures. Because of their flexible structural units and adjustable interactions between components, luminescent metal–organic framework sensors have been developed for the detection of inorganic ions and organic pollutants in recent years.[6–9] To achieve luminescent sensors with high

[a] *School of Materials Science and Engineering, Central South University, Changsha, 410083, China. E-mail: rosesunqz@csu.edu.cn*
[b] *Key Laboratory of Catalysis and Materials Sciences of the State Ethnic Affairs Commission & Ministry of Education, College of Chemistry and Material Science, South-Central Minzu University, Wuhan, 430074, China.*
E-mail: 3092809@mail.scuec.edu.cn

selectivity and sensitivity, many researchers have exploited large π-conjugated ligands containing multiple N- and O-donor atoms.[10–16] Results indicated that the intermolecular interaction between MOFs and guest molecules is an important factor deciding the MOF's sensing capability.[17–20] However, the mechanism underlying the modulation of the luminescence detection performance of MOFs through this interaction has not yet been explored.

As is known, the interaction mainly depends on the electron density of N- and O-donor atoms, which is subject to the coordination environment in coordination polymers. In other words, the interaction between MOFs and guest molecules can be revealed through the effect of different coordination environments of donor atoms on fluorescence detection. Thus, in this work, two luminescent Cd(II) coordination polymers with N, O and S donor atoms were constructed based on the 5-[(dimethylamino)thioxomethoxy]-1,3-benzenedicarboxylic acid ligand for Fe³⁺ detection. The crystal structures of the two polymers were determined to clarify the coordination environment of the functional groups. In addition, the fluorescence detection performances of the two polymers were performed and compared.

Experimental section

Materials, devices and crystal data characterization

The ligand 5-[(dimethylamino)thioxomethoxy]-1,3-benzenedicarboxylic acid (H$_2$L) was synthesized according to

our earlier report.[21] All the reagents and solvents used for the synthesis and analysis were commercially available. Elemental analysis (C, H contents) was performed using a Perkin-Elmer 240 analyzer. IR spectra were recorded using a Vector 22 Bruker spectrophotometer with KBr pellets in the 4000–400 cm^{-1} region at room temperature. Thermogravimetric analyses (TGA) were performed using a Perkin-Elmer thermal analyzer at a heating rate of 10 °C min^{-1} in a nitrogen atmosphere. Powder X-ray diffraction (PXRD) patterns were recorded using a Rigaku D/max-2550 X-ray diffractometer with graphite-monochromatized Cu-Kα (1.54056 Å) radiation at 40 kV/250 mA at room temperature. Luminescence spectra of the samples were recorded using a FLS920 spectrophotometer with a xenon arc lamp as the light source at room temperature. X-ray photoelectron spectra (XPS) were recorded using a Thermo Scientific Escalab 250Xi spectrometer. ^{1}H nuclear magnetic resonance (^{1}H NMR) spectra were recorded using a Mercury plus 600 spectrometer. UV-vis spectra were recorded using a Shimadzu UV-2550 double-beam spectrophotometer at ambient temperature.

Synthesis of [CdL(dpa)]·2.5H$_2$O (1)

A mixture of Cd(NO$_3$)$_2$·4H$_2$O (31 mg, 0.1 mmol), H$_2$L (30 mg, 0.1 mmol), and dpa (17 mg, 0.1 mmol) in 2 mL DMF/H$_2$O (v/v, 1 : 1) was sealed in a Teflon-lined autoclave and heated to 120 °C for 60 h, and then gradually cooled down to room temperature. Yellow crystals were obtained. Yield: 0.04 g (67%, based on Cd(NO$_3$)$_2$·4H$_2$O). Anal. calcd for C$_{21}$H$_{23}$N$_4$O$_{7.50}$SCd: C, 42.29; H, 3.86; N, 9.40%. Found: C, 42.36; H, 3.76; N, 9.47%. IR (KBr, cm^{-1}) 3446(m), 2924(m), 1668(m), 1593(s), 1441(w), 1371(m), 1348(s), 1285(w), 1210(m), 1137(w), 1102(vw), 1055(vw), 1013(m), 901(vw), 865(vw), 812(w), 778(w), 736(w), 591(w), 536(w), 435(w).

Synthesis of Cd$_2$L$_2$(2,2′-bpy)$_2$ (2)

A mixture of Cd(NO$_3$)$_2$·4H$_2$O (31 mg, 0.1 mmol), H$_2$L (30 mg, 0.1 mmol), and 2,2′-bipyridine (2,2′-bpy) (16 mg, 0.1 mmol) in 2 mL DMF/H$_2$O (v/v, 1 : 1) was sealed in a Teflon-lined autoclave and heated to 120 °C for 60 h, and then gradually cooled down to room temperature. Yellow crystals were obtained. Yield: 0.07 g (65%, based on Cd(NO$_3$)$_2$·4H$_2$O). Anal. calcd for C$_{42}$H$_{34}$N$_6$O$_{10}$S$_2$Cd$_2$: C, 47.07; H, 3.20; N, 7.84%. Found: C, 47.26; H, 3.23; N, 7.78%. IR (KBr, cm^{-1}) 3416(m), 2925(m), 2851(w), 1607(m), 1543(s), 1439(m), 1366(s), 1348(s), 1287(w), 1234(w), 1135(m), 1098(w), 1059(vw), 1013(w), 927(vw), 811(w), 769(m), 729(m), 647(vw), 589(vw), 441(w).

X-ray crystallography

X-ray diffraction intensity data of compounds 1 and 2 were measured using a Bruker SMART CCD diffractometer equipped with a graphite-monochromatized Mo Kα radiation source (λ = 0.71073 Å) using an ω–φ scan mode at 296(2) K. The data sets were corrected for absorption by a multi-scan technique. The structures were solved *via* a direct method and refined by full-matrix least squares on F^2.[22] All non-hydrogen atoms were refined with anisotropic thermal

displacement coefficients. The hydrogen atoms were assigned with isotropic displacement factors. In compound 1, two water molecules were refined as disordered. The details of crystal data, selected bond lengths and angles, and hydrogen bond ranges for compounds 1 and 2 are listed in Tables 1, S1 and S2,† respectively. The crystallographic data of 1 and 2 have been deposited with the Cambridge Crystallographic Data Center. CCDC reference numbers: 2080883 for 1 and 2080887 for 2, respectively.

Photoluminescence experiments

In a typical experiment, compound 1 (5.0 mg) was finely ground and immersed in 3.0 mL solvent, ultrasonicated for 6 h, and then aged for 2 days to form a stable suspension for luminescence measurements.

Results and discussion

Crystal structure of compound 1

Compound 1 crystallizes in a monoclinic system, $P2_1/n$ space group. The crystallographic analysis revealed that the structure of 1 consists of one Cd^{2+} ion, one dpa and one L^{2-} ligand. As depicted in Fig. 1a, Cd1 has a distorted octahedral geometry, with the equational plane formed by three oxygen donors (O1B, O2B and O5) and one nitrogen atom (N2), and the axial position occupied by one carboxylate oxygen atom (O4) and one nitrogen atom (N4C). The lengths of Cd–O and Cd–N bonds are found in the ordinary range (Table S1†). The L^{2-} ligand is fully deprotonated and each carboxylate group displays a chelated coordination mode to coordinate with one Cd(II) center. The dpa ligands exhibit ditopic linkers, leaving the amino groups uncoordinated. A nearly square

Table 1 Crystal data and structure refinement details for compounds 1 and 2

| Compounds	1	2
Empirical formula	C$_{21}$H$_{23}$CdN$_4$O$_{7.50}$S	C$_{42}$H$_{34}$Cd$_2$N$_6$O$_{10}$S$_2$
Formula weight	595.89	1071.67
Crystal system	Monoclinic	Triclinic
Space group	$P2_1/n$	$P\bar{1}$
a (Å)	11.1116(7)	10.3270(10)
b (Å)	14.8127(9)	13.8387(13)
c (Å)	15.3395(9)	18.3399(18)
α (°)	90	102.5480(10)
β (°)	101.8020(10)	101.1410(10)
γ (°)	90	102.3540(10)
V (Å^3)	2471.4(3)	2418.9(4)
Z	4	2
D (g cm^{-3})	1.602	1.471
Mu (mm^{-1})	1.018	1.023
$F(0\,0\,0)$	1204	1072
Unique reflections	3718	6043
Observed reflections	4341	8476
R_{int}	0.0218	0.0312
Final R indices [$I > 2\sigma(I)$]	$R_1 = 0.0374$	$R_1 = 0.0360$
	w$R_1 = 0.1064$	w$R_1 = 0.0800$
R indices (all data)	$R_1 = 0.0448$	$R_1 = 0.0601$
	w$R_2 = 0.1109$	w$R_2 = 0.0848$
Goodness-of-fit on F^2	1.029	1.036

Paper
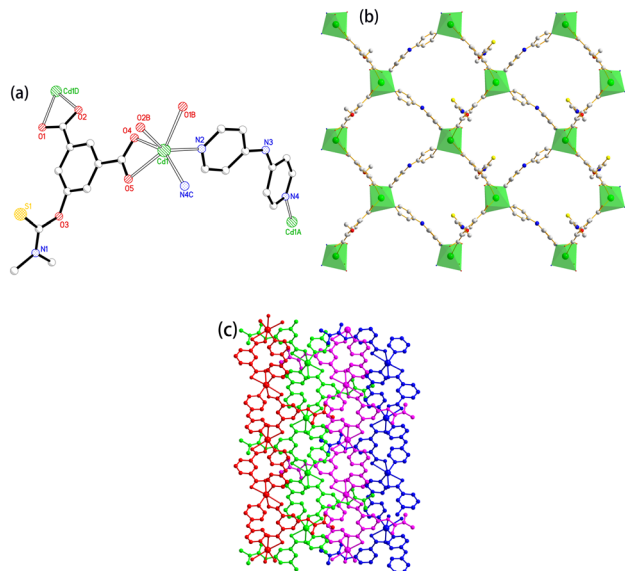
Fig. 1 (a) Coordination environment of Cd^{2+}, L^{2-} and dpa in **1**. Symmetry codes: a: $-x + 0.5$, $y - 0.5$, $-z - 0.5$; b: $-x + 0.5$, $y + 0.5$, $-z + 0.5$; c: $-x + 0.5$, $y + 0.5$, $-z - 0.5$; d: $-x + 0.5$, $y - 0.5$, $-z + 0.5$. (b) Two-dimensional plane along the *bc* plane. (c) (Dimethylamino) thioxomethoxy groups protruding into the grids of the neighboring layers.

grid is constructed by four Cd^{2+} ions, two dpa and two L^{2-} ligands with a Cd···Cd distance of 14.81×15.34 Å^2. The grids extend into a porous two-dimensional (2D) layer (Fig. 1b) with the (dimethylamino)thioxomethoxy groups hanging above and below the layer (Fig. S1a†). In addition, the hanging (dimethylamino)thioxomethoxy groups protrude into the grids of the neighboring layers to form an interdigitated motif (Fig. 1c). The layers are further connected by O–H···O, N–H···O and C–H···O hydrogen bonds (Table S2, Fig. S1b†).

Crystal structure of compound 2

Compound **2** crystallizes in a triclinic system, $P\bar{1}$ space group. In **2**, each asymmetric unit contains two crystallographically independent Cd^{2+} ions, two L^{2-} ligands and two 2,2′-bpy ligands. Cd1 and Cd2 are both coordinated by four carboxylate oxygen atoms from three different L^{2-} ligands and two nitrogen atoms from one 2,2′-bpy (Fig. 2a). Each L^{2-} ligand bridges three Cd^{2+} ions through a μ_3-O, O′, (η^2-O″, O‴) coordination mode. Unlike the ditopic coordination of dpa in

1, 2,2′-bpy in **2** acts as an anchored ligand to coordinate with Cd^{2+} ions. In compound **2**, two Cd^{2+} ions are connected by two carboxyl to construct a dimer, and the dimers are further linked by L^{2-} ligands to generate a ladder-like chain with the (dimethylamino)thioxomethoxy groups hanging on the two sides of the chains (Fig. 2b). The chains are assembled through C–H···O and C–H···S hydrogen bonds (Fig. S2†).

Comparison of recognition sites between 1 and 2

According to our previous study,[23–25] the electron donor atoms such as the uncoordinated nitrogen atoms, oxygen atoms and sulfur atoms can act as the recognition sites for the detection of metal ions. For **1**, the 2D layer with a porosity of nearly 14.81×15.34 Å^2 enables the (dimethylamino)thioxomethoxy groups to protrude into the grids of the adjacent layers, which enlarge the steric hindrance of the recognition sites and impede the interactions between the metal ions and the electron donor atoms. While for **2**, no enlarged steric hindrance of the recognition sites is observed as the hanging (dimethylamino) thioxomethoxy groups on the two sides of the chain are not interfered by the neighbouring chains (Fig. S2a†).

Thermal and water stability of 1 and 2

The thermogravimetric analysis (TGA) of compounds **1** and **2** was performed to verify the thermal stability (Fig. S3†). For **1**, the first mass loss of 7.38% at a temperature from 30 to 140 °C could be attributed to the release of all lattice water molecules (calcd 7.55%). Then it remained stable until about 225 °C. After that, it began to decompose quickly. For **2**, the framework did not decompose until the temperature reached about 215 °C. In addition, samples **1** and **2** were immersed in water for 24 h. In addition, the powder X-ray diffraction (PXRD) patterns (Fig. S4†) of immersed **1** and **2** were the same as those of compounds **1** and **2**. Therefore, compounds **1** and **2** are stable in water.

Solid-state fluorescence

The fluorescence spectra of H_2L, dpa, 2,2′-bpy and compounds **1** and **2** were investigated in the solid state at room temperature. As shown in Fig. 3, compounds **1** and **2** exhibit intensive emission with fluorescence peaks at 461
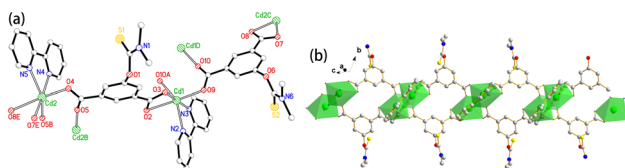

Fig. 2 (a) Coordination environment of Cd^{2+}, L^{2-} and 2,2′-bpy in **2**. Symmetry codes: a: $-x$, $-y$, $-z + 1$; b: $-x + 1$, $-y$, $-z + 2$; c: $x - 1$, y, $z - 1$; d: $-x$, $-y$, $-z + 1$; e: $x + 1$, y, $z + 1$. (b) One-dimensional ladder-like chain.
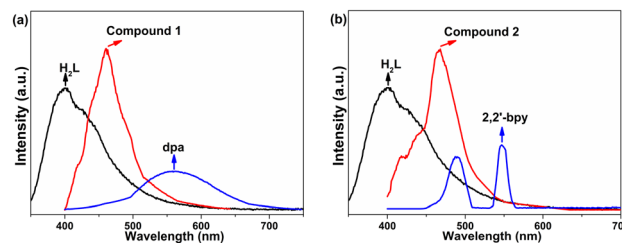

Fig. 3 Solid-state emission spectra of compounds **1** (a) and **2** (b), H_2L, dpa and 2,2′-bpy at room temperature. $\lambda_{ex} = 355$ nm for **1** and **2**, 400 nm for H_2L, and 410 nm for dpa.

and 468 nm (λ_{ex} = 355 nm), respectively, while the free ligands show emission with fluorescence peaks at 400 nm for H_2L (λ_{ex} = 325 nm), 560 nm for dpa (λ_{ex} = 410 nm) and 489 and 546 nm for 2,2′-bpy (λ_{ex} = 331 nm). Compared with the free ligands, an obvious shift of compound **1** (**2**) is observed, which can attribute to both the coordination of metal centers and ligands[26–28] and the emission of ligand-to-metal charge-transfer (LMCT).[29,30] Furthermore, as the six-coordinated Cd(II) ions in both compounds are d^2sp^3 hybridized, they will accept charge from the ligand with 5d orbitals. The lifetimes are τ_1 = 1.22 ± 0.01 μs (56.0%) and τ_2 = 9.83 ± 0.02 μs (44.0%) for **1** and τ_1 = 1.07 ± 0.02 μs (47.7%) and τ_2 = 9.28 ± 0.02 μs (52.3%) for **2**.

Detection of Fe³⁺ ions

Compounds **1** and **2** as fluorescent probes for the detection of Fe^{3+} were investigated. The luminescence behavior of **1** (**2**) dispersed in different solvents such as acetone, CCl_4, CH_2Cl_2, MeCN, DMF, DMSO, EtOH, H_2O, MeOH, THF, and NB (nitrobenzene) was first investigated at room temperature (Fig. 4 and S5†). It displayed that the fluorescence was almost completely quenched by the addition of NB. In consideration of practical applications, the detection of metal ions was performed in water solutions.

Typically, 5 mg of the crystalline powder of **1** (**2**) was dispersed in 3 mL metal cationic aqueous solutions (Ba^{2+}, Zn^{2+}, Mg^{2+}, Co^{2+}, Na^+, K^+, Mn^{2+}, Cd^{2+}, Ni^{2+}, Sr^{2+}, Pb^{2+}, Ca^{2+}, Ag^+, Hg^{2+}, Fe^{3+}, and Cu^{2+}) followed by ultrasonic treatment for 20 min to form suspensions. The PXRD and IR spectra manifested that compounds **1** and **2** are stable after sonication, as shown in Fig. S6 and S7.† The fluorescence spectra of both **1** and **2** (λ_{ex} = 355 nm) were quenched upon the addition of Fe^{3+} (Fig. 5). The counterion for Ba^{2+}, Ca^{2+}, Fe^{3+}, Hg^{2+}, Mg^{2+}, K^+, Na^+, Mn^{2+} and Sr^{2+} ions was Cl^-, and the counterion for Ag^+, Cd^{2+}, Co^{2+}, Cu^{2+}, Ni^{2+}, Pb^{2+} and Zn^{2+} ions was NO_3^-. After the addition of Na^+ salt solution containing Cl^- and NO_3^- ions (Fig. S8†), the luminescence intensities of **1** (**2**), **1** (**2**) + NaCl and **1** (**2**) + NaNO₃ are almost the same. This indicated that the nature of the anions had a negligible effect on the luminescence intensity of **1** (**2**).

The selectivity experiments displayed that both **1** and **2** showed high selectivity toward Fe^{3+} ions in the presence of interfering ions (Fi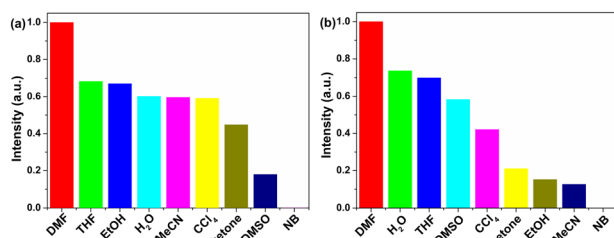g. S9†). The titration experiments (Fig. S10†) were conducted, and the fluorescence quenching efficiency of Fe^{3+} was calculated using the Stern–Volmer (S–V) equation, $(I_0/I) = 1 + K_{sv}[C] = 1 + K_q\tau_0[C]$,[31] where I_0 and I are the fluorescent intensities of **1** (**2**) before and after the addition of Fe^{3+}, respectively. K_{sv} is the quenching constant (M^{-1}), C is the molar concentration of Fe^{3+}, τ_0 is the average life of the fluorescent substance without a quencher (calculated using the equation $(\alpha_1\tau_1^2 + \alpha_2\tau_2^2)/(\alpha_1\tau_1 + \alpha_2\tau_2)$), valued 8.65×10^{-6} s for **1** and 8.48×10^{-6} s for **2**, and K_q is the rate constant in the process of double molecule quenching. As shown in Fig. 6, the emission ratio (I_0/I) of both **1** and **2** for Fe^{3+} exhibited a good linear correlation at a lower concentration (Fig. 6 inset) and the quenching constants (K_{sv}) of **1** and **2** were 2.96×10^4 M^{-1} and 3.31×10^4 M^{-1}, respectively. In addition, the slope became steep at higher concentrations of Fe^{3+} ions, which could be attributed to the combination of static and dynamic quenching processes between metal ions and MOFs,[32] or self-absorption or energy transfer.[33] The K_q values of **1** and **2** were 3.42×10^9 M^{-1} s^{-1} and 3.90×10^9 M^{-1} s^{-1} ($<2.0 \times 10^{10}$ M^{-1} s^{-1}), respectively, and this could be attributed to dynamic quenching.[31] The fluorescence lifetime changes before and after sensing, further verifying the dynamic quenching (Fig. S11†). From Fig. S12,† it is clear that **1** (**2**) exhibited a fast response toward Fe^{3+} within a few seconds. The limit of detection (LOD) values of **1** and **2** for Fe^{3+} were calculated to be 6.40×10^{-5} mM and 7.65×10^{-5} mM respectively using the following equation: LOD = $3\sigma/k$ (Fig. S13, Tables S3 and S4†). In the case of Fe^{3+}, the normal ranges for the detection limit and K_{sv} values are 10^{-5}–10^{-8} M and 10^3–10^5 M^{-1}, respectively. Obviously, the data in this work are better or comparable to those of the reported Cd-based MOF luminescent probes
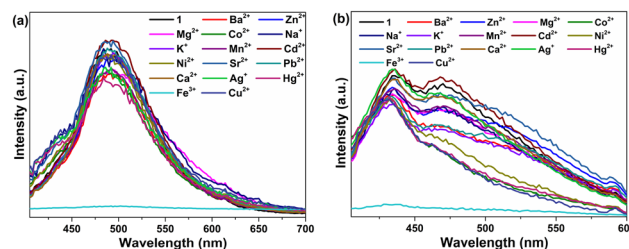

Fig. 5 Emission spectra of **1** (a) and **2** (b) immersed in water containing metal ions (condition: 5 mg **1**, 3 mL H_2O, and 0.02 mmol metal ions).

Fig. 4 Fluorescence response of **1** (a) and **2** (b) in different solvents at room temperature.
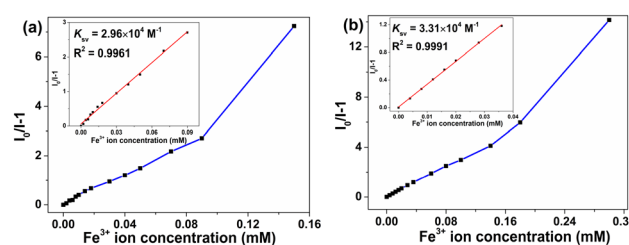

Fig. 6 S–V plot of **1** (a) and **2** (b) at different concentrations of Fe^{3+} ions (insets: linear correlation at lower concentrations).

Table 2 Comparison of Cd-MOF-based luminescent probes for the detection of Fe^{3+} ions

Compounds	K_{sv}	LOD	Ref.
$[Cd_2(L)(bib)_{0.5}(H_2O)_3]_n \cdot 1.75n(H_2O)$	4.653×10^4 L mol^{-1}	2.96×10^{-5} mol L^{-1}	34
LCU-109	5.71×10^4 M^{-1}	0.0043 ppm	35
$\{[Cd(ttc)(H_2O)] \cdot H_2O\}_n$	—	5.34×10^{-8} M	36
$[Cd(PAM)(4\text{-bpdb})_{1.5}] \cdot DMF$	3.5×10^4 M^{-1}	0.3 μM	37
$[Cd(BIM)_2Cl_2]_n \cdot BIM$	9.59×10^3 M^{-1}	2.51×10^{-5} mol L^{-1}	38
Cd-MOF	3.663×10^5 M^{-1}	3.86 μM	39
$[Cd_2(H_2O)(4\text{-PDCA})_2]_n$	2.72×10^3 mol L	9.80×10^{-6} mol L^{-1}	40
$[Cd_{1.5}(NTB)(bipy)_{0.5}]_n$	4.3×10^4 M^{-1}	2.19×10^{-6} M	41
$[CdL(dpa)] \cdot 2.5H_2O$	2.96×10^4 M^{-1}	6.40×10^{-5} mM	This work
$Cd_2L_2(2,2'\text{-bpy})_2$	3.31×10^4 M^{-1}	7.65×10^{-5} mM	This work

(Table 2).[34–41] In addition, the K_{sv} and LOD values of **1** are lower than that of **2**, which may be attributed to the enlarged steric hindrance of **1**. Interestingly, the Cd-MOF[39] with a higher K_{sv} value also exhibited a 1D chain structure, and the 3dpu ligand containing an uncoordinated nitrogen atom appeared above and below the chain. The structural similarity between Cd-MOF and compound **2** further indicates that the decreased steric hindrance of recognition sites is advantageous for the detection of Fe^{3+} ions. In the presence of anti-interference metal ions such as Ba^{2+}, Zn^{2+}, Mg^{2+}, Co^{2+}, Na^+, K^+, Mn^{2+}, Cd^{2+}, Ni^{2+}, Sr^{2+}, Pb^{2+}, Ca^{2+}, Ag^+, Hg^{2+} and Cu^{2+}, the recyclable performance of **1** (**2**) for the detection of Fe^{3+} ions was conducted. As shown in Fig. S14,† the fluorescence intensity of **1** (**2**) slightly reduced after washing with water and ethanol.

Mechanism for the detection of Fe^{3+}

The mechanism for the luminescence quenching of different metal ions generally includes ionic exchange, collapse or change of structure, competitive absorption, and coordination interactions between Fe^{3+} and ligands.[23–25] The cationic exchange and the structure decomposition were excluded because of the good agreement of the PXRD patterns of **1** (**2**) and the Fe^{3+}-incorporated **1** (**2**) (Fig. S4†). Fig. S15† displays the UV-visible spectrum of the metal salts overlapped with the fluorescence spectrum of **1** and **2**. The strong absorption band of Fe^{3+} certainly exhibited a maximum overlap with both the excitation and emission spectra of **1** (**2**) compared with that of other metal ions, which indicated that competitive absorption did exist between Fe^{3+} and **1** (**2**). Meanwhile, the competitive absorption mainly existed between the UV spectra of metal ions and the excited spectra of **1** (**2**). The overlap between the UV spectra of metal ions and the excited spectra of **1** is a little larger.

In order to explore the effects of the recognition sites on the fluorescence detection of Fe^{3+}, the XPS analysis of **1** (**2**) before and after the absorption of Fe^{3+} ions was performed. As illustrated in Fig. S16,† two new peaks of Fe $2p_{1/2}$ and Fe $2p_{3/2}$ were detected in both **1** and **2** after the detection of Fe^{3+}, suggesting that Fe^{3+} has been adsorbed onto the two compounds, respectively. The XPS spectra of

N 1s, O 1s and S 2p before and after the detection of Fe^{3+} were further analyzed. As shown in Fig. 7a, the N 1s spectrum of **1** could be dissected into three peaks at binding energies of 399.95, 399.24 and 398.80 eV, attributed to the nitrogen atom in the pyridine group, amine group and dimethylamino group, respectively. After Fe^{3+} adsorption, the former two peaks shifted to 400.16 and 399.73 eV, respectively, which could be assigned to the chelation between the nitrogen atoms and Fe^{3+} ions.[42,43] However, for the dimethylamino group, there was almost no change after the addition of Fe^{3+}. According to the crystal structure of **1**, the (dimethylamino)thioxomethoxy groups protruding into the adjacent grids enlarged the steric hindrance, which might impede their coordination interactions with Fe^{3+} ions. For **2**, its N 1s spectrum displays two peaks at 399.54 and 398.88 eV, corresponding to the nitrogen atom in the pyridine group and dimethylamino group, respectively. After the addition of Fe^{3+}, the peaks shifted to 399.84 and 399.46 eV, respectively (Fig. 7b). The peak–peak displacement values of N 1s in **2** were larger than that of **1** (Table S5†). The peaks of O 1s at 533.13 and 530.95 eV indicated the presence of carboxyl
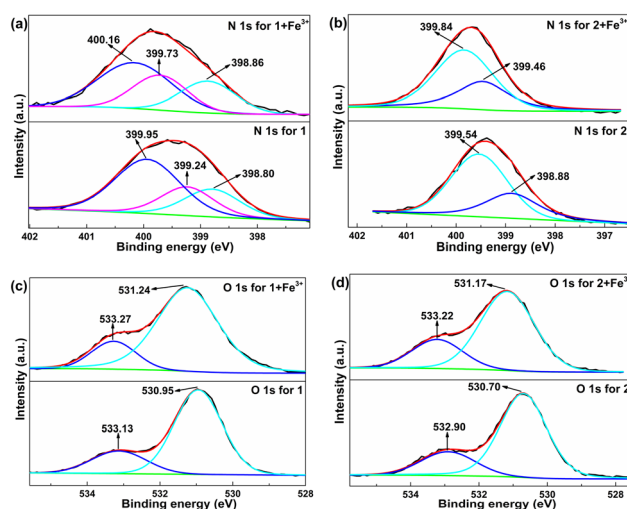

Fig. 7 XPS survey of N 1s of compounds **1** (a) and **2** (b) before and after binding with Fe^{3+}. XPS survey of O 1s of compounds **1** (c) and **2** (d) before and after binding with Fe^{3+}.

and alkyl oxygen in **1**, respectively. After the addition of Fe^{3+}, the O 1s peak for the carboxylic group shifted to 533.27 eV and the alkyl oxygen shifted to 531.24 eV, demonstrating that the oxygen atoms bound with Fe^{3+} (Fig. 7c).[44,45] Accordingly, the O 1s spectra of **2** exhibited two peaks at 532.9 and 530.7 eV before Fe^{3+} addition, and the corresponding peaks shifted to 533.22 and 531.17 eV after Fe^{3+} addition (Fig. 7d). The S 2p peak in **1** shifted from 161.69 to 161.76 eV before and after the addition of Fe^{3+}, and the peak in **2** changed from 161.61 to 162.02 eV. Moreover, the peak–peak displacement values of O 1s (S 2p) in **2** were larger than that of **1** (Table S5†). The above-mentioned results could be explained by the change in electron density and the effect of steric hindrance around the groups. On the one hand, the easily transferred electrons from the conductive band of **1** (**2**) to the 3d orbitals of half-filled Fe^{3+} caused fluorescence quenching.[44,46] The binding of Fe^{3+} and the groups incorporating nitrogen (oxygen or sulfur) atoms prompted electron transfer, leading to the loss of electron density at the functional groups, which, in turn, increased the binding energy.[47] On the other hand, the enlarged steric hindrance in **2** blocked the coordination interactions between Fe^{3+} and the functional groups containing N, O and S, which resulted in smaller peak–peak displacement values.

From the FTIR spectra (Fig. S18†), a new peak at 474 cm^{-1} emerged in **1** incorporating Fe^{3+}. An obvious difference was also observed between **2** and **2** incorporating Fe^{3+} below 625 cm^{-1}. The distinction in the low wavenumber region could be attributed to the interactions between Fe^{3+} and the functional groups of the compounds, which were in accordance with the results of XPS.

Conclusion

In summary, to explore the effects of the recognition sites of MOFs on fluorescence detection, two luminescent Cd(II) coordination polymers based on 5-[(dimethylamino)thioxomethoxy]-1,3-benzenedicarboxylic acid have been developed for the detection of Fe^{3+}. The detection performance of both **1** and **2** could be explained by the synergistic effect of competitive absorption and the coordination interactions. In addition, the detection performance of **2** was better than that of **1**. This mainly attributed to the interactions between Fe^{3+} and the multiple N, O and S active sites of the polymers as competitive absorption of **1** and **2** caused a little difference. The detailed investigation manifested that the protruding (dimethylamino)thioxomethoxy groups enlarged the steric hindrance of **1** and blocked the coordination of the recognition sites with Fe^{3+} ions. The result revealed the delicate relationship between the structure and the function of luminescent MOF materials. Studies on the effects of multiple functional sites of other MOFs on the detection of metal ions are now underway in our laboratory.

Data availability

The data supporting the findings of this study are available from the corresponding author upon request.

Author contributions

Senlin Li: investigation and writing – original draft. Yanan Gu: investigation and validation. Bo Zhao: investigation and validation. Haocheng Cai: writing – review and editing. Zhuo Zhao: data curation. Qiaozhen Sun: conceptualization, supervision and writing – review and editing. Bingguang Zhang: writing – review and editing.

Conflicts of interest

The authors declare no competing financial interest.

Acknowledgements

Notes and references

1 I. T. Y. Lam, S.-J. Choi, D. Lu and Y. Kim, Functionalized metal-organic frameworks for heavy metal ion removal from water, *Nanoscale*, 2023, **15**, 10189–10205.

2 S. N. Nangare, S. R. Patil, A. G. Patil, Z. G. Khan, P. K. Deshmukh, R. S. Tade, M. R. Mahajan, S. B. Bari and P. O. Patil, Structural design of nanosize metal-organic framework based sensors for detection of organophosphorus pesticides in food and water samples: current challenges and future prospects, *J. Nanostruct. Chem.*, 2022, **12**, 729–764.

3 J. H. Song and D. W. Kang, Hazardous nitroaromatic explosives detection by emerging porous solid sensors, *Coord. Chem. Rev.*, 2023, **492**, 215279.

4 M. K. Wilsey, T. Taseska, Z. Meng, W. Yu and A. M. Mueller, Advanced electrocatalytic redox processes for environmental remediation of halogenated organic water pollutants, *Chem. Commun.*, 2023, **59**, 11895–11922.

5 S. Zhao, J. Xiao, T. Zheng, M. Liu, H. Wu and Z. Liu, Highly Selective and Sensitive Detection of PO43- Ions in Aqueous Solution by a Luminescent Terbium Metal-Organic Framework, *ACS Omega*, 2019, **4**, 16378–16384.

6 S. S. Shafqat, M. Rizwan, M. Batool, S. R. Shafqat, G. Mustafa, T. Rasheed and M. N. Zafar, Metal organic frameworks as promising sensing tools for electrochemical detection of persistent heavy metal ions from water matrices: A concise review, *Chemosphere*, 2023, **318**, 137920.

7 M. Wagner, K.-Y. A. Lin, W.-D. Oh and G. Lisak, Metal-organic frameworks for pesticidal persistent organic pollutants detection and adsorption - A mini review, *J. Hazard. Mater.*, 2021, **413**, 125325.

8 B. Jie, H. Lin, Y. Zhai, J. Ye, D. Zhang, Y. Xie, X. Zhang and Y. Yang, Mechanism, design and application of fluorescent recognition based on metal organic frameworks in pollutant detection, *Chem. Eng. J.*, 2023, **454**, 139931.

9 D. Zhao, S. Yu, W.-J. Jiang, Z.-H. Cai, D.-L. Li, Y.-L. Liu and Z.-Z. Chen, Recent Progress in Metal-Organic Framework Based Fluorescent Sensors for Hazardous Materials Detection, *Molecules*, 2022, **27**, 2226.

10 B. Mohan, Priyanka, G. Singh, A. Chauhan, A. J. L. Pombeiro and P. Ren, Metal-organic frameworks (MOFs) based luminescent and electrochemical sensors for food contaminant detection, *J. Hazard. Mater.*, 2023, **453**, 131324.

11 D. Luo, J. Huang, Y. Jian, A. Singh, A. Kumar, J. Liu, Y. Pan and Q. Ouyang, Metal-organic frameworks (MOFs) as apt luminescent probes for the detection of biochemical analytes, *J. Mater. Chem. B*, 2023, **11**, 6802–6822.

12 J. Jin, J. Xue, Y. Liu, G. Yang and Y.-Y. Wang, Recent progresses in luminescent metal-organic frameworks (LMOFs) as sensors for the detection of anions and cations in aqueous solution, *Dalton Trans.*, 2021, **50**, 1950–1972.

13 Z.-Q. Shi, N.-N. Ji and H.-L. Hu, Luminescent triphenylamine-based metal-organic frameworks: recent advances in nitroaromatics detection, *Dalton Trans.*, 2020, **49**, 12929–12939.

14 M. S. More, G. A. Bodkhe, F. Singh, B. N. Dole, M.-L. Tsai, T. Hianik and M. D. Shirsat, Chemiresistive and chem-FET Sensor: π-d conjugated metal-organic framework for ultra-sensitive and selective carbon monoxide detection, *Synth. Met.*, 2023, **296**, 117357.

15 B. Zhu, L. Zhu, S. Deng, Y. Wan, F. Qin, H. Han and J. Luo, A fully π-conjugated covalent organic framework with dual binding sites for ultrasensitive detection and removal of divalent heavy metal ions, *J. Hazard. Mater.*, 2023, **459**, 132081.

16 Y. Song, Y. Meng, K. Chen, G. Huang, S. Li and L. Hu, Novel electrochemical sensing strategy for ultrasensitive detection of tetracycline based on porphyrin/metal phthalocyanine-covalent organic framework, *Bioelectrochemistry*, 2024, **156**, 108630.

17 X. Yu, A. A. Ryadun, D. I. Pavlov, T. Y. Guselnikova, A. S. Potapov and V. P. Fedin, Highly Luminescent Lanthanide Metal-Organic Frameworks with Tunable Color for Nanomolar Detection of Iron(III), Ofloxacin and Gossypol and Anti-counterfeiting Applications, *Angew. Chem.*, 2023, **62**, e202306680.

18 Z. Li, G. Dai, F. Luo, Y. Lu, J. Zhang, Z. Chu, P. He, F. Zhang and Q. Wang, An electrochemical sensor for bacterial lipopolysaccharide detection based on dual functional Cu^{2+}-modified metal-organic framework nanoparticles, *Microchim. Acta*, 2020, **187**, 415.

19 C. Hong, L. Li, J.-Y. Zou, L. Zhang and S.-Y. You, A turn-on fluorescent Zn(II) metal-organic framework sensor for quantitative anthrax biomarker detection, *Dalton Trans.*, 2023, **52**, 6067–6076.

20 L. Liu, X. Chen, J. Qiu and C. Hao, New insights into the nitroaromatics-detection mechanism of the luminescent metal-organic framework sensor, *Dalton Trans.*, 2015, **44**, 2897–2906.

21 Y. Gu, S. Li, Q. Sun and B. Zhang, Controlled synthesis, structure and luminescent property of a 3D layered-pillared zinc(II) coordination polymer based on a newly designed ligand, *J. Mol. Struct.*, 2023, **1274**, 134598.

22 G. M. Sheldrick, Crystal structure refinement with SHELXL, *Acta Crystallogr., Sect. C: Struct. Chem.*, 2015, **71**, 3–8.

23 B. Zhao, J. Lu, H. Liu, S. Li, Q. Sun and B. Zhang, Design and synthesis of a turn-off fluorescent sensor based on a multifunctional Zn(II) coordination polymer for the detection of Fe^{3+}, Hg^{2+} and 4-nitrophenol, *CrystEngComm*, 2024, **26**, 1319–1327.

24 Y.-N. Gu, J.-F. Lu, H. Liu, B. Zhao, X.-H. Zhou, Y.-Q. Zhao, Q.-Z. Sun and B. G. Zhang, Two Eu^{3+} Based Complexes Containing Uncoordinated Lewis Basic Pyridyl Sites and Chemical Sensing of 4 Nitrophenol and Fe^{3+} ions, *Cryst. Growth Des.*, 2022, **22**, 4874–4884.

25 B. Zhao, S.-L. Li, Y.-N. Gu, Q.-Z. Sun and H. Liu, A stable turn-off fluorescence sensor for nitroaromatic explosives and Fe^{3+} detection based on a 3D strontium coordination polymer, *J. Mol. Struct.*, 2022, **1270**, 133944.

26 W.-D. Li, S.-S. Chen, S.-S. Han and Y. Zhao, The syntheses, structures, and properties of metal-organic frameworks based on mixed multi-N donor and carboxylate ligands, *J. Solid State Chem.*, 2020, **283**, 121133.

27 R. Sun, Y.-Z. Li, J. Bai and Y. Pan, Synthesis, structure, water induced reversible crystal-to-amorphous transformation, and luminescence properties of novel cationic spacer-filled 3D transition metal supramolecular frameworks from N,′,N″-tris(carboxymethyl)-1,3,5-benzenetricarboxamide, *Cryst. Growth Des.*, 2007, **7**, 890–894.

28 L.-Y. Zhang, J.-P. Zhang, Y.-Y. Lin and X.-M. Chen, Syntheses, structures, and photoluminescence of three coordination polymers of cadmium dicarboxylates, *Cryst. Growth Des.*, 2006, **6**, 1684–1689.

29 M. D. Allendorf, C. A. Bauer, R. K. Bhakta and R. J. T. Houk, Luminescent metal-organic frameworks, *Chem. Soc. Rev.*, 2009, **38**, 1330–1352.

30 V. W. W. Yam, Molecular design of transition metal alkynyl complexes as building blocks for luminescent metal-based materials: Structural and photophysical aspects, *Acc. Chem. Res.*, 2002, **35**, 555–563.

31 Y. Li, F. Gao, F. Gao, F. Shan, J. Bian and C. Zhao, Study on the Interaction between 3 Flavonoid Compounds and α-Amylase by Fluorescence Spectroscopy and Enzymatic Kinetics, *J. Food Sci.*, 2009, **74**, C199–C203.

32 M. Peng, K. Huang, X. Li, D. Han, Q. Qiu, L. Jing and D. Qin, Tetra(4-imidazoylphenyl)ethylene based metal-organic frameworks for highly selective detection of TNP and Fe^{3+}, *J. Solid State Chem.*, 2019, **280**, 120993.

33 Y.-E. Yao, B. Yang and L. Wang, A water stable Zn(II)-MOF for luminescent detection of Fe^{3+} ion and clinic nursing values on the anaphylactic shock by up-regulating the α receptor expression, *J. Polym. Res.*, 2021, **28**, 57.

34 G.-L. Wen, W.-P. Wu, F.-W. Wang, D.-F. Liu, X.-L. Wang, J.-W. Rong and Y.-Y. Wang, An excellent thermostable dual-functionalized 3D fsx-type Cd(II) MOF for the highly selective detection of Fe^{3+} ions and ten nitroaromatic explosives, *CrystEngComm*, 2021, **23**, 6171–6179.

35 J. Li, Y.-X. Zhao, Q. Wu, H. Yang, J. Lu, H.-Y. Ma, S.-N. Wang and Y.-W. Li, A Cd-MOF fluorescence sensor with dual functional sites for efficient detection of metal ions in multifarious water environments, *CrystEngComm*, 2021, **23**, 8392–8403.

36 W. Liu, H.-I. Cui, J. Zhou, Z.-t. Su, Y.-z. Zhang, X.-I. Chen and E. I. Yue, Synthesis of a Cd-MOF Fluorescence Sensor and Its Detection of Fe3+, Fluazinam, TNP, and Sulfasalazine Enteric-Coated Tablets in Aqueous Solution, *ACS Omega*, 2023, **8**, 24635–24643.

37 R. Lv, Z. Chen, X. Fu, B. Yang, H. Li, J. Su, W. Gu and X. Liu, A highly selective and fast-response fluorescent probe based on Cd-MOF for the visual detection of Al^{3+} ion and quantitative detection of Fe^{3+} ion, *J. Solid State Chem.*, 2018, **259**, 67–72.

38 C. Su and F. Guo, A Cd(II)-based MOF as a dual-responsive luminescent probe for highly selective detection of Fe^{3+} cation and nitrofurantoin, *Inorg. Chem. Commun.*, 2021, **125**, 108427.

39 Q. Wen, J.-L. Chen, J.-F. Song, S.-Y. Zhou, H.-Y. Zhu and X.-Q. Zhang, Synthesis of novel coordination polymer Cd-MOF and fluorescent probe detection of Fe^{3+}, $Cr_2O_7^{2-}$, and ceftriaxone sodium (CRO), *J. Mol. Struct.*, 2024, **1300**, 137235.

40 J.-H. Gao, P.-P. Huang, Z.-J. Zhang, F.-W. Tian, J. Ge, X.-Y. Cao, J. Liu, D. Wang, N. Zheng, J.-F. Lu and B. Liu, A new 3D Cd-MOF with 2fold interpenetrated as "turn-on/turn-off" fluorescent sensor for selective and sensitive detection of Cu^{2+}, Al^{3+} and Fe^{3+} ions, *J. Mol. Struct.*, 2024, **1299**, 137162.

41 H. Yang, D. Qi, X. Si, Z. Yan, L. Guo, C. Shao, W. Zhang and L. Yang, One novel Cd-MOF as a highly effective multi-functional luminescent sensor for the detection of Fe^{3+}, Hg^{2+}, Cr^{VI}, Aspartic acid and Glutamic acid in aqueous solution, *J. Solid State Chem.*, 2022, **310**, 123008.

42 X. Luo, L. Ding and J. Luo, Adsorptive removal of Pb(II) ions from aqueous samples with amino-functionalization of metal-organic frameworks MIL-101(Cr), *J. Chem. Eng. Data*, 2015, **60**, 1732–1743.

43 S.-W. Lv, J.-M. Liu, C.-Y. Li, N. Zhao, Z.-H. Wang and S. Wang, A novel and universal metal-organic frameworks sensing platform for selective detection and efficient removal of heavy metal ions, *Chem. Eng. J.*, 2019, **375**, 122111.

44 Y. Zhao, H. Ouyang, S. Feng, Y. Luo, Q. Shi, C. Zhu, Y.-C. Chang, L. Li, D. Du and H. Yang, Rapid and selective detection of Fe (III) by using a smartphone-based device as a portable detector and hydroxyl functionalized metal-organic frameworks as the fluorescence probe, *Anal. Chim. Acta*, 2019, **1077**, 160–166.

45 H. Xu, Y. Dong, Y. Wu, W. Ren, T. Zhao, S. Wang and J. Gao, An-OH group functionalized MOF for ratiometric Fe^{3+} sensing, *J. Solid State Chem.*, 2018, **258**, 441–446.

46 M. Kumar, R. Kumar and V. Bhalla, Optical chemosensor for Ag^+, Fe^{3+} and cysteine: information processing at molecular level, *Org. Lett.*, 2011, **13**, 366–369.

47 A. Pankajakshan, D. Kuznetsov and S. Mandal, Ultrasensitive Detection of Hg(II) Ions in Aqueous Medium Using Zinc-Based Metal-Organic Framework, *Inorg. Chem.*, 2019, **58**, 1377–1381.